

On small deformation interfacial debonding in composite materials containing multi-coated particles

Roohollah Hashemi¹, Daniel W Spring¹ and
Glaucio H Paulino^{1,2}

Abstract

This paper presents an integrated theoretical and computational investigation into the macroscopic behavior of composite materials containing multi-phase reinforcing particles with simultaneous nonlinear debonding along the micro-constituent interfaces. The interfacial debonding is characterized by the nonlinear Park–Paulino–Roesler potential-based cohesive zone model. The extended Mori–Tanaka method is employed as the basis for the theoretical model, which enables micromechanical formulations for composite materials with high particle volume fractions. The computational analysis is performed using a three-dimensional finite element-based cohesive zone model with intrinsic cohesive elements. To place the generality and robustness of the proposed technique in perspective, we consider several examples of composite materials with single or double separation along the interfaces of coated particles. The effects of many microstructural parameters, such as the geometry of the microstructure, the location of debonding, the material properties of the coating layer (i.e. homogenous and functionally graded coatings), and the fracture parameters, are comprehensively investigated by both theoretical and numerical approaches. We verify that both theoretical and numerical results agree well with one another in estimating the macroscopic constitutive relationship of corresponding composite materials. The strong dependence of the overall response of composite materials on their microstructure is well recognized for all hardening, snap-back, and softening stages.

Keywords

Multi-phase particles, nonlinear separation, Park–Paulino–Roesler cohesive zone model, homogeneous coating, hollow particles, functionally graded coating

Introduction and motivation

In characterizing the macroscopic behavior of composite materials, the behavior of the material in the vicinity of the reinforcing particles is of utmost importance. In other words, the microgeometry and associated property of each phase of the particle ensemble, as well as the interface conditions, contributes to the macroscopic behavior of composite materials. In general, a particle ensemble in a composite material consists of an inner most phase (called core particle) enclosed by several phases along the interfacial zone (called coating layers). Nowadays, coating techniques are often applied to the particles of a composite material to meet various desired specifications. For instance, single or multiple coating layer(s) are employed to reduce or redistribute residual tensile stresses between the particles and the matrix and, consequently, to prevent matrix cracking during the cool-down process. In addition, coatings are

often applied to protect reinforcing particles against aggressive corrosive agents or to improve thermomechanical behavior, electroelastic constants, or electrical conductivity of composite materials. On the other hand, as a result of chemical interactions, a transition phase (coating layer) may form between the core particle and the matrix during the manufacturing and processing of composite materials. Even though these coating layers are typically microscopic, they

¹Department of Civil and Environmental Engineering, University of Illinois at Urbana-Champaign, Urbana, IL, USA

²School of Civil and Environmental Engineering, Georgia Institute of Technology, Atlanta, GA, USA

Corresponding author:

Glaucio H Paulino, School of Civil and Environmental Engineering, Georgia Institute of Technology, 790 Atlantic Drive, Atlanta, GA 30332, USA.
Email: paulino@gatech.edu

can greatly influence the macroscopic behavior of composite materials.

Because of the abovementioned potential gains that coated particles can deliver, several investigators have paid special attention to this topic. Recently, Qu et al.¹ visualized and investigated the mechanical influence of this coating layer in rubber-carbon black nanocomposites. They illustrate, using torsional harmonic atomic force microscopy, that the coating layer in these composites is an order of magnitude stiffer than the surrounding rubber matrix and has a thickness anywhere from 10% to 50% the radius of the particle inclusions. They also illustrate that the stiffness of the interphase is not constant but varies as a function of the distance from the particle, as illustrated in Figure 1.

Prediction of the macroscopic behavior of composites consisting of multi-phase inhomogeneities, perfectly bonded to the surrounding matrix, has been investigated extensively during the past two decades.^{2–11} However, the perfect bonding assumption across the constituents' interfaces is sometimes a limiting idealization. Interfacial debonding can occur within microconstituents of a composite material either during the manufacturing process or due to damage evolution when the composite is loaded.^{12–17}

An examination of the literature reveals that several researchers have linked particle-matrix interface behavior with the macroscopic behavior of composite materials; see, for example, Benveniste,¹⁸ Achenbach and Zhu,¹⁹ Sangani and Mo,²⁰ Nie and Basaran,²¹ Schjodt and Pyrz,²² and Lee and Pyo.²³ These researchers characterize imperfect bonding at the particle-matrix interface as linear spring-type models, thus a fully debonded stage cannot be reached in their studies. Alternatively, several analytical and numerical investigations have

been conducted on the interface debonding process using nonlinear cohesive models, which assume a phenomenological relation between the traction and separation at the interface. For instance, Xu and Needleman²⁴ investigated void nucleation along the interface in conjunction with an exponential cohesive relation. Using a bilinear cohesive relation, Tan et al.¹⁴ studied the effect of nonlinear interface debonding on the macroscopic constitutive behavior of high explosive materials subjected to hydrostatic tension. In a separate study, they extended their method to the case of uniaxial tension.^{25,26} Carpinteri et al.²⁷ investigated snap-back instabilities in microstructured composites under uniaxial displacement boundary conditions in conjunction with a contact formulation which handles cohesive forces. Ngo et al.²⁸ estimated the macroscopic constitutive behavior of composite materials using the potential-based Park–Paulino–Roesler (PPR) cohesive model for interfacial debonding. Their investigation integrates a theoretical micromechanics model together with a finite element-based numerical model. Recently, Othmani et al.²⁹ proposed an Eshelby's equivalent inclusion solution in order to model interface debonding of spherical particles using a cohesive zone approach. All of these studies are pertinent to composites containing single-phase inhomogeneities; none is concerned with multi-coated particles. To the best of the authors' knowledge, the nonlinear interfacial debonding along different constituent phases of multi-coated particles, which is of great value in understanding the physical behavior of high-performance composites, has not been addressed in the literature. This is the main focus of the present contribution.

In this paper, we present theoretical and numerical investigations into the macroscopic behavior of

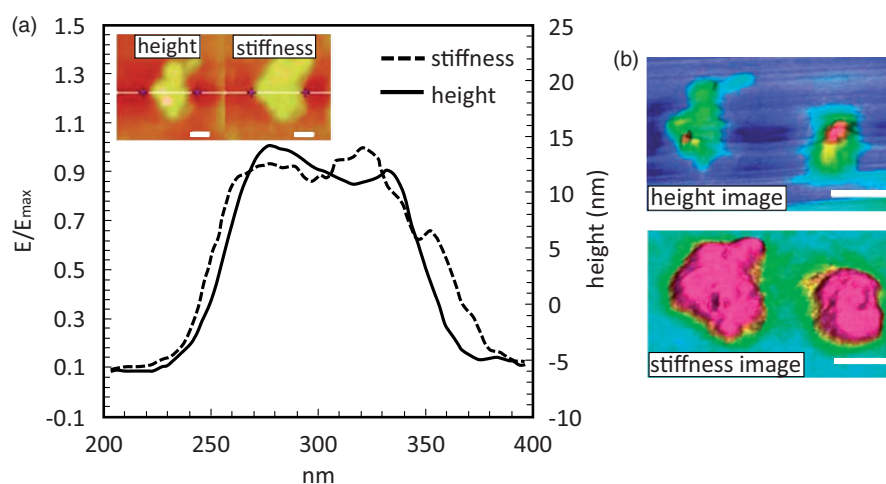


Figure 1. (a) Normalized particle profiles measured on torsional harmonic atomic force microscopy height and stiffness maps. Scale bar = 50 nm and (b) three-dimensional rendering of height and stiffness images. Scale bar = 100 nm. (Images from Qu et al.¹)

composite materials with multi-phase inhomogeneities accounting for simultaneous interfacial debonding across different phases of a particles' ensemble. To account for nonlinear debonding, the PPR potential-based cohesive zone model is used. Three key emphasis of this study are: (1) extending the Mori–Tanaka method to account for nonlinear debonding along all interfaces of a multi-coated particle, (2) implementing a three-dimensional finite element-based cohesive zone model for the computational simulation of debonding, and (3) investigating the influence of microstructure parameters on the macroscopic behavior of composite materials through a comprehensive theoretical and numerical parametric study. Accordingly, the remainder of the paper is organized as follows. First, we present the problem statement and formulation, where we formulate our theoretical micromechanics model accounting for nonlinear separation at all interfaces of composite microstructures. Then, we present an integrated theoretical and numerical investigation of several examples of microstructures of practical and theoretical importance. Then, we discuss and motivate the extension of this work to additional loading conditions. Finally, the key findings of the paper are summarized.

Problem statement and formulation

Consider a representative volume element (RVE), with volume V , of a composite material containing a random distribution of spherical, multi-coated particles with different sizes and/or material properties. We assume the matrix, particles, and coating layers as linear elastic. As depicted in Figure 2(a), the β th particle ensemble ($\beta = 1, 2, \dots, P$, where P is the number of particles in the composite) consists of an inner core, Ω_1^β , surrounded by an arbitrary number of coating layers, Ω_γ^β

($\gamma = 2, 3, \dots, N_\beta$, where N_β is the number of layers in the particle ensemble). The interface between the γ th and $(\gamma + 1)$ th coating layers of the β th particle ensemble is denoted as Γ_γ^β ($\gamma = 1, 2, \dots, N_\beta - 1$), and the interface between the outer most coating, $\Omega_{N_\beta}^\beta$, and the surrounding matrix is denoted as $\Gamma_{N_\beta}^\beta$. The volume fraction of each particle phase, $f^{\Omega_\gamma^\beta}$, is denoted as $V^{\Omega_\gamma^\beta}/V$.

The average stresses in the matrix, $\bar{\sigma}^m$, and in the γ th phase of the β th particle ensemble, $\bar{\sigma}^{\Omega_\gamma^\beta}$, are defined as

$$\bar{\sigma}^m = \frac{1}{V^m} \int_{V^m} \sigma^m dV \quad \text{and} \quad \bar{\sigma}^{\Omega_\gamma^\beta} = \frac{1}{V^{\Omega_\gamma^\beta}} \int_{V^{\Omega_\gamma^\beta}} \sigma^{\Omega_\gamma^\beta} dV \quad (1)$$

respectively, where σ^m is the microscopic stress in the matrix, and $\sigma^{\Omega_\gamma^\beta}$ is the microscopic stress in the corresponding phase. Then, the average, or macroscopic, stress in the RVE, $\bar{\sigma}$, is expressed in terms of these averaged quantities as

$$\bar{\sigma} = (1 - f)\bar{\sigma}^m + \sum_{\beta=1}^P \left(\sum_{\gamma=1}^{N_\beta} f^{\Omega_\gamma^\beta} \bar{\sigma}^{\Omega_\gamma^\beta} \right) \quad (2)$$

where $f = \sum_{\beta=1}^P \sum_{\gamma=1}^{N_\beta} f^{\Omega_\gamma^\beta}$. Similarly, suppose that the average strains in the matrix and in phase Ω_γ^β are denoted as

$$\bar{\varepsilon}^m = \frac{1}{V^m} \int_{V^m} \varepsilon^m dV \quad \text{and} \quad \bar{\varepsilon}^{\Omega_\gamma^\beta} = \frac{1}{V^{\Omega_\gamma^\beta}} \int_{V^{\Omega_\gamma^\beta}} \varepsilon^{\Omega_\gamma^\beta} dV \quad (3)$$

respectively. The average, or macroscopic, strain in the RVE, $\bar{\varepsilon}$, is related to $\bar{\varepsilon}^m$ and $\bar{\varepsilon}^{\Omega_\gamma^\beta}$ by

$$\bar{\varepsilon} = (1 - f)\bar{\varepsilon}^m + \sum_{\beta=1}^P \left(\sum_{\gamma=1}^{N_\beta} f^{\Omega_\gamma^\beta} \bar{\varepsilon}^{\Omega_\gamma^\beta} + f^{\Gamma_\gamma^\beta} \bar{\varepsilon}^{\Gamma_\gamma^\beta} \right) \quad (4)$$

where $f^{\Gamma_\gamma^\beta} = 4\pi R_{\Gamma_\gamma^\beta}^3/3V$, and $R_{\Gamma_\gamma^\beta}$ denotes the radius of interface Γ_γ^β , and $\bar{\varepsilon}^{\Gamma_\gamma^\beta}$ represents the average

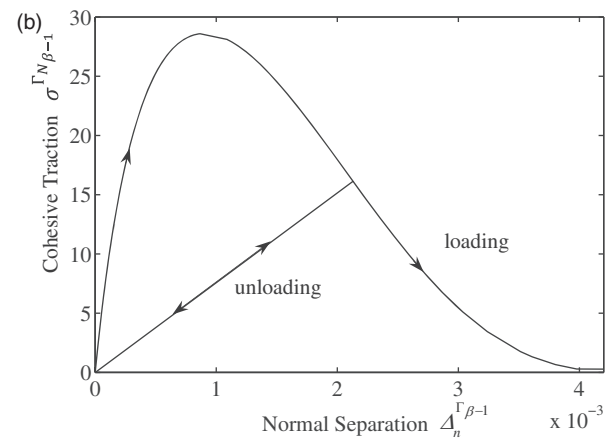
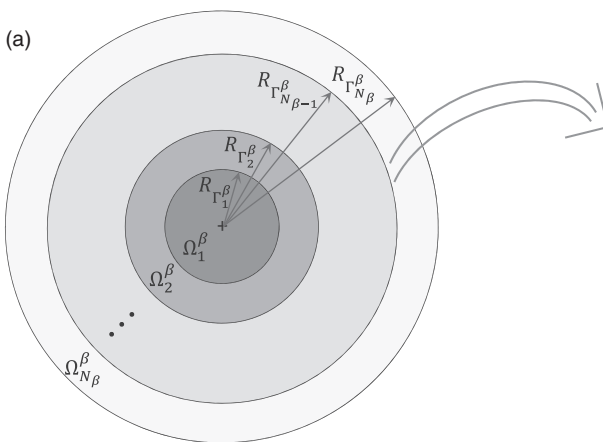


Figure 2. (a) Microgeometry and microconstituent phases of β th particle ensemble and (b) illustrative cohesive relation of normal separation along a typical interface, $\Gamma_{N_\beta-1}^\beta$.

contribution from the separation along interface Γ_γ^β . This contribution is related to the displacement discontinuity

$$\Delta \Gamma_\gamma^\beta = \begin{cases} u^{\Omega_{\gamma+1}^\beta} - u^{\Omega_\gamma^\beta}, & \text{for } \gamma = 1, 2, \dots, N_\beta - 1, \\ u^m - u^{\Omega_\gamma^\beta}, & \text{for } \gamma = N_\beta, \end{cases} \quad (5)$$

across the interface, Γ_γ^β , by

$$\bar{\varepsilon}^{\Gamma_\gamma^\beta} = \frac{1}{2V\Gamma_\gamma^\beta} \int_{S\Gamma_\gamma^\beta} (\Delta \Gamma_\gamma^\beta \otimes n + n \otimes \Delta \Gamma_\gamma^\beta) dS, \quad (6)$$

where u^m and $u^{\Omega_\gamma^\beta}$ are the displacements on the associated debonding interface from the matrix side and particle side, respectively, and n is the unit outward normal vector on the interface (following positive sign convention).

The average strains in the matrix, and in the γ th phase of the β th particle ensemble, are related to the associated average stresses by $\bar{\varepsilon}^m = M^m : \bar{\sigma}^m$ and $\bar{\varepsilon}^{\Omega_\gamma^\beta} = M^{\Omega_\gamma^\beta} : \bar{\sigma}^{\Omega_\gamma^\beta}$, where M^m and $M^{\Omega_\gamma^\beta}$ are the elastic compliance tensors of the matrix and the corresponding phase, respectively. Then, the macroscopic strain can be rewritten in terms of the macroscopic stress as

$$\bar{\varepsilon} = M^m : \bar{\sigma} + \sum_{\beta=1}^P \left(\sum_{\gamma=1}^{N_\beta} f^{\Omega_\gamma^\beta} (M^{\Omega_\gamma^\beta} - M^m) : \bar{\sigma}^{\Omega_\gamma^\beta} + f^{\Gamma_\gamma^\beta} \bar{\varepsilon}^{\Gamma_\gamma^\beta} \right) \quad (7)$$

This expression indicates that the macroscopic strain can be thought of as the combination of strain due to the average stress applied to the matrix (first term), the perturbation strain due to induced stresses in the particle phases (second term), together with the strain due to the simultaneous debonding across the interfaces (third term). Note that equations (2) and (7) are exact general relations which hold for composite materials with multi-coated particles experiencing concurrent debonding across the interfaces.

To find the macroscopic stress–strain relationship, some approximations need to be made for the evaluation of $\bar{\sigma}^m$, $\bar{\sigma}^{\Omega_\gamma^\beta}$, and $\bar{\varepsilon}^{\Omega_\gamma^\beta}$ in terms of $\bar{\sigma}$ and $\bar{\varepsilon}$. In order to be able to proceed with an analytical solution for this complex problem, we consider the case of a composite material subjected to a state of hydrostatic tension, $\bar{\sigma} = \bar{\sigma} \mathbf{I}$, where \mathbf{I} is the second-order identity tensor. For spherical particles, the average strain due to the displacement discontinuity at interface Γ_γ^β is

$$\bar{\varepsilon}_{ii}^{\Gamma_\gamma^\beta} = \frac{1}{V\Gamma_\gamma^\beta} \int_{S\Gamma_\gamma^\beta} \Delta_n^{\Gamma_\gamma^\beta} dS = 3\Delta_n^{\Gamma_\gamma^\beta} / R_{\Gamma_\gamma^\beta} \quad (8)$$

where $\Delta_n^{\Gamma_\gamma^\beta}$ is the average radial separation at interface, Γ_γ^β . Tensorial equations (2) and (7) are rewritten as the

following scalar equations

$$\bar{\sigma} = (1 - f)\bar{\sigma}^m + \sum_{\beta=1}^P \left(\sum_{\gamma=1}^{N_\beta} f^{\Omega_\gamma^\beta} \bar{\sigma}^{\Omega_\gamma^\beta} \right) \quad (9)$$

$$\bar{\varepsilon} = \frac{1 - 2\nu^m}{E^m} \bar{\sigma} + \sum_{\beta=1}^P \left\{ \sum_{\gamma=1}^{N_\beta} f^{\Omega_\gamma^\beta} \left(\frac{1 - 2\nu^{\Omega_\gamma^\beta}}{E^{\Omega_\gamma^\beta}} - \frac{1 - 2\nu^m}{E^m} \right) \bar{\sigma}^{\Omega_\gamma^\beta} + f^{\Gamma_\gamma^\beta} \Delta_n^{\Gamma_\gamma^\beta} / R_{\Gamma_\gamma^\beta} \right\} \quad (10)$$

where (E^m, ν^m) and $(E^{\Omega_\gamma^\beta}, \nu^{\Omega_\gamma^\beta})$ are the elastic moduli and Poisson’s ratios of the matrix and corresponding phase, respectively. The average stresses in the matrix and in the γ th phase of the β th particle ensemble are defined as $\bar{\sigma}^m = \bar{\sigma}_{ii}^m/3$ and $\bar{\sigma}^{\Omega_\gamma^\beta} = \bar{\sigma}_{ii}^{\Omega_\gamma^\beta}/3$, respectively.

To obtain the constitutive relation between $\bar{\sigma}$ and $\bar{\varepsilon}$, we adopt the extended Mori–Tanaka method to determine both the average stress, $\bar{\sigma}^{\Omega_\gamma^\beta}$, and the displacement separation, $\Delta_n^{\Gamma_\gamma^\beta}$, in terms of the macroscopic stress, $\bar{\sigma}$. The main idea of this method is to relate the microscopic stress to the average stress in the matrix, instead of the macroscopic stress, in the RVE.^{30–32} As schematically illustrated in Figure 3, following the Mori–Tanaka approach, we consider the β th particle ensemble as a single inhomogeneity in an infinite matrix subjected to remote hydrostatic tension, $\bar{\sigma}^m$. Then, we decompose the multi-phase particle into the core particle together with a series of hollow elastic spheres subjected to uniform radial stress across their inner and outer boundaries. The stresses acting on the interfaces are obtained from a cohesive relation, which describes the nonlinear debonding at the particle interfaces. In the present study, as illustrated in Figure 2(b), we use the PPR potential-based model for the description of interfacial debonding, which consistently relates the cohesive traction, $\sigma^{\Gamma_\gamma^\beta}$, to the normal separation, $\Delta_n^{\Gamma_\gamma^\beta}$, along interface, Γ_γ^β , of a particle ensemble.^{28,33} The constitutive cohesive relation at interface Γ_γ^β is written as:

- For loading across the interface

$$\sigma^{\Gamma_\gamma^\beta} = \frac{\phi_n}{\delta_n} \left(\frac{\alpha}{m} \right)^m \left(1 - \frac{\Delta_n^{\Gamma_\gamma^\beta}}{\delta_n} \right)^{\alpha-1} \left(\frac{m}{\alpha} - \frac{\Delta_n^{\Gamma_\gamma^\beta}}{\delta_n} \right)^{m-1} (m + \alpha) \frac{\Delta_n^{\Gamma_\gamma^\beta}}{\delta_n} \quad (11)$$

- For unloading/reloading across the interface

$$\sigma^{\Gamma_\gamma^\beta} = \sigma^{\Gamma_\gamma^\beta}(\Delta_{n\max}^{\Gamma_\gamma^\beta}) \left(\frac{\Delta_n^{\Gamma_\gamma^\beta}}{\Delta_{n\max}^{\Gamma_\gamma^\beta}} \right) \quad (12)$$

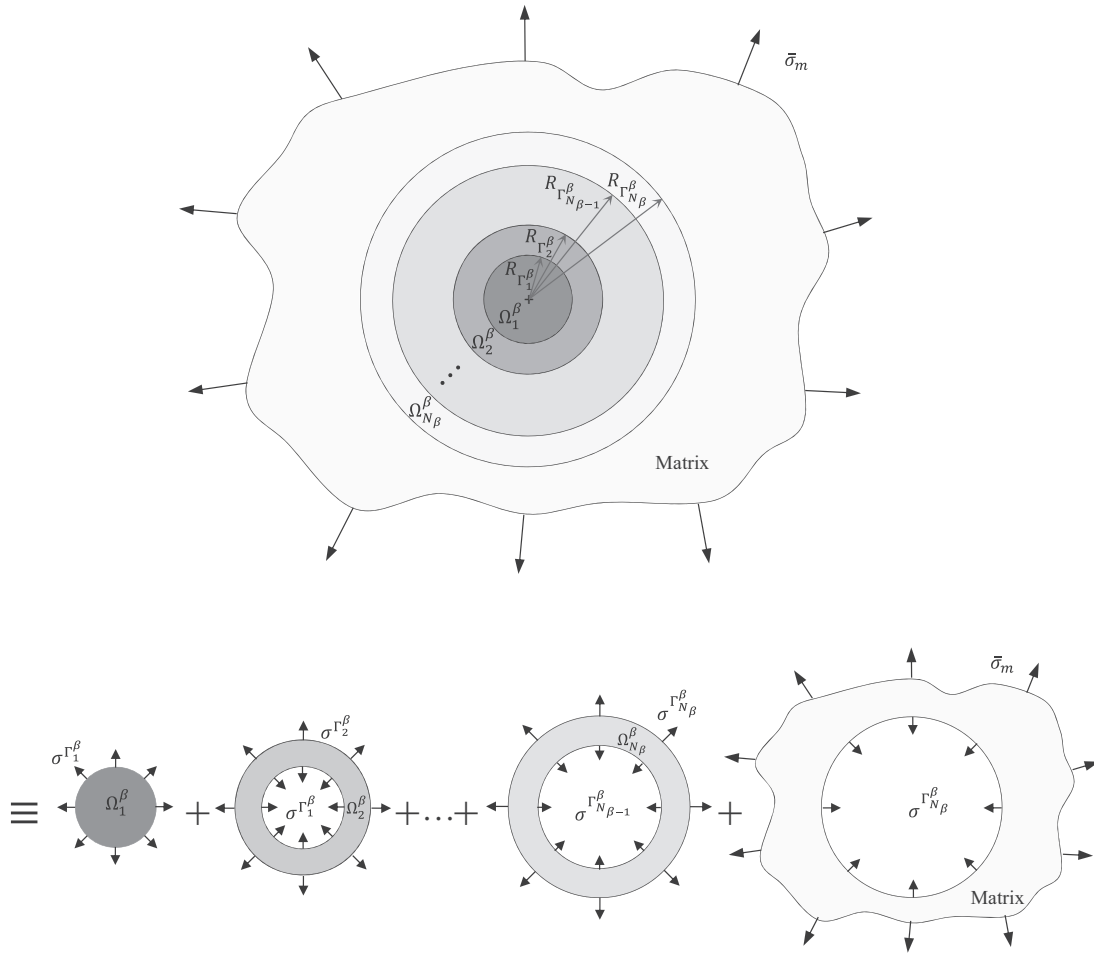


Figure 3. Decomposition of a typical multi-inhomogeneity system into the core particle and its coating layers, subjected to cohesive tractions. Hydrostatic loading is considered.

in which characteristic fracture parameters of α , m , δ_n , and ϕ_n are the shape parameter, nondimensional exponent, final opening separation length, and fracture energy of the debonding interface, respectively.^{34,35} With the abovementioned decomposition scheme, together with the elastic solution for a hollow sphere under applied internal and external stresses,^{36,37} the microscopic stress in the particle core and its surrounding coating layers is obtained in terms of cohesive tractions, as

$$\bar{\sigma}^{\Omega_\gamma^\beta} = \begin{cases} \sigma^{\Gamma_\gamma^\beta}, & \text{for } \gamma = 1, \\ \left(\sigma^{\Gamma_{\gamma-1}^\beta} R_{\Gamma_{\gamma-1}^\beta}^3 - \sigma^{\Gamma_\gamma^\beta} R_{\Gamma_\gamma^\beta}^3 \right) / \left(R_{\Gamma_{\gamma-1}^\beta}^3 - R_{\Gamma_\gamma^\beta}^3 \right) \\ \text{for } \gamma = 2, 3, \dots, N_\beta. \end{cases} \quad (13)$$

Then, the equation for the constitutive relation between the macroscopic stress and macroscopic strain of

the composite material is obtained in terms of $\Delta_n^{\Gamma_\gamma^\beta}$ and $\sigma^{\Gamma_\gamma^\beta}$, as

$$\bar{\sigma} = (1-f)\bar{\sigma}^m + \sum_{\beta=1}^P \left(f^{\Omega_\beta^\beta} \sigma^{\Gamma_1^\beta} + \sum_{\gamma=2}^{N_\beta} f^{\Omega_\gamma^\beta} \left(\sigma^{\Gamma_{\gamma-1}^\beta} R_{\Gamma_{\gamma-1}^\beta}^3 - \sigma^{\Gamma_\gamma^\beta} R_{\Gamma_\gamma^\beta}^3 \right) / \left(R_{\Gamma_{\gamma-1}^\beta}^3 - R_{\Gamma_\gamma^\beta}^3 \right) \right) \quad (14)$$

$$\bar{\varepsilon} = \frac{1-2\nu^m}{E^m} \bar{\sigma} + \sum_{\beta=1}^P \left\{ f^{\Omega_\beta^\beta} \left(\frac{1-2\nu^{\Omega_\beta^\beta}}{E^{\Omega_\beta^\beta}} - \frac{1-2\nu^m}{E^m} \right) \sigma^{\Gamma_1^\beta} + \sum_{\gamma=2}^{N_\beta} f^{\Omega_\gamma^\beta} \left(\frac{1-2\nu^{\Omega_\gamma^\beta}}{E^{\Omega_\gamma^\beta}} - \frac{1-2\nu^m}{E^m} \right) \times \left(\sigma^{\Gamma_{\gamma-1}^\beta} R_{\Gamma_{\gamma-1}^\beta}^3 - \sigma^{\Gamma_\gamma^\beta} R_{\Gamma_\gamma^\beta}^3 \right) / \left(R_{\Gamma_{\gamma-1}^\beta}^3 - R_{\Gamma_\gamma^\beta}^3 \right) + f^{\Gamma_\gamma^\beta} \Delta_n^{\Gamma_\gamma^\beta} / R_{\Gamma_\gamma^\beta} \right\} \quad (15)$$

Similarly, using the theory of elasticity,^{36,37} the radial displacement of each phase of the particle ensemble at

its inner and outer debonding interfaces can be obtained. In other words, by substitution of the corresponding displacement into equation (5), the normal separation at each interface of the multi-phase system is computed as:

- Normal separation at particle-coating interface, Γ_1^β

$$\begin{aligned} \Delta_n^{\Gamma_1^\beta} = & \frac{1 - 2\nu^{\Omega_2^\beta}}{E^{\Omega_2^\beta} \left(R_{\Gamma_1^\beta}^3 - R_{\Gamma_2^\beta}^3 \right)} \left(R_{\Gamma_1^\beta}^3 \sigma^{\Gamma_1^\beta} - R_{\Gamma_2^\beta}^3 \sigma^{\Gamma_2^\beta} \right) R_{\Gamma_1^\beta}^\beta \\ & + \frac{1 + \nu^{\Omega_2^\beta}}{2E^{\Omega_2^\beta} \left(R_{\Gamma_1^\beta}^3 - R_{\Gamma_2^\beta}^3 \right)} \times \left(\sigma^{\Gamma_1^\beta} - \sigma^{\Gamma_2^\beta} \right) R_{\Gamma_2^\beta}^3 R_{\Gamma_1^\beta}^\beta \\ & - \frac{1 - 2\nu^{\Omega_1^\beta}}{E^{\Omega_1^\beta}} \sigma^{\Gamma_1^\beta} R_{\Gamma_1^\beta}^\beta \end{aligned} \tag{16}$$

- Normal separation at debonding interface Γ_γ^β ($\gamma = 2, \dots, N_\beta - 1$)

$$\begin{aligned} \Delta_n^{\Gamma_\gamma^\beta} = & \frac{1 - 2\nu^{\Omega_{\gamma+1}^\beta}}{E^{\Omega_{\gamma+1}^\beta} \left(R_{\Gamma_\gamma^\beta}^3 - R_{\Gamma_{\gamma+1}^\beta}^3 \right)} \left(R_{\Gamma_\gamma^\beta}^3 \sigma^{\Gamma_\gamma^\beta} - R_{\Gamma_{\gamma+1}^\beta}^3 \sigma^{\Gamma_{\gamma+1}^\beta} \right) R_{\Gamma_\gamma^\beta}^\beta \\ & - \frac{1 - 2\nu^{\Omega_\gamma^\beta}}{E^{\Omega_\gamma^\beta} \left(R_{\Gamma_{\gamma-1}^\beta}^3 - R_{\Gamma_\gamma^\beta}^3 \right)} \left(R_{\Gamma_{\gamma-1}^\beta}^3 \sigma^{\Gamma_{\gamma-1}^\beta} - R_{\Gamma_\gamma^\beta}^3 \sigma^{\Gamma_\gamma^\beta} \right) R_{\Gamma_{\gamma-1}^\beta}^\beta \\ & + \frac{1 + \nu^{\Omega_{\gamma+1}^\beta}}{2E^{\Omega_{\gamma+1}^\beta} \left(R_{\Gamma_\gamma^\beta}^3 - R_{\Gamma_{\gamma+1}^\beta}^3 \right)} \left(\sigma^{\Gamma_\gamma^\beta} - \sigma^{\Gamma_{\gamma+1}^\beta} \right) R_{\Gamma_{\gamma+1}^\beta}^3 R_{\Gamma_\gamma^\beta}^\beta \\ & - \frac{1 + \nu^{\Omega_\gamma^\beta}}{2E^{\Omega_\gamma^\beta} \left(R_{\Gamma_{\gamma-1}^\beta}^3 - R_{\Gamma_\gamma^\beta}^3 \right)} \left(\sigma^{\Gamma_{\gamma-1}^\beta} - \sigma^{\Gamma_\gamma^\beta} \right) R_{\Gamma_\gamma^\beta}^3 R_{\Gamma_{\gamma-1}^\beta}^\beta \end{aligned} \tag{17}$$

- Normal separation at coating-matrix interface, $\Gamma_{N_\beta}^\beta$

$$\begin{aligned} \Delta_n^{\Gamma_{N_\beta}^\beta} = & R_{\Gamma_{N_\beta}^\beta}^\beta \left[3(1 - \nu^m) \bar{\sigma}^m - (1 + \nu^m) \sigma^{\Gamma_{N_\beta}^\beta} \right] / 2E^m \\ & - \frac{1 - 2\nu^{\Omega_{N_\beta}^\beta}}{E^{\Omega_{N_\beta}^\beta} \left(R_{\Gamma_{N_\beta-1}^\beta}^3 - R_{\Gamma_{N_\beta}^\beta}^3 \right)} \left(R_{\Gamma_{N_\beta-1}^\beta}^3 \sigma^{\Gamma_{N_\beta-1}^\beta} - R_{\Gamma_{N_\beta}^\beta}^3 \sigma^{\Gamma_{N_\beta}^\beta} \right) \\ & \times R_{\Gamma_{N_\beta}^\beta}^\beta - \frac{1 + \nu^{\Omega_{N_\beta}^\beta}}{2E^{\Omega_{N_\beta}^\beta} \left(R_{\Gamma_{N_\beta-1}^\beta}^3 - R_{\Gamma_{N_\beta}^\beta}^3 \right)} \left(\sigma^{\Gamma_{N_\beta-1}^\beta} - \sigma^{\Gamma_{N_\beta}^\beta} \right) \\ & \times R_{\Gamma_{N_\beta}^\beta}^3 R_{\Gamma_{N_\beta-1}^\beta}^\beta \end{aligned} \tag{18}$$

Then, the average stress in the matrix, $\bar{\sigma}^m$, is obtained in terms of the displacement jump and the

traction at the corresponding interfaces, i.e. $\Gamma_{N_\beta}^\beta$ and $\Gamma_{N_\beta-1}^\beta$, as

$$\begin{aligned} \bar{\sigma}^m = & \frac{2E^m}{3(1 - \nu^m)} \left\{ \Delta_n^{\Gamma_{N_\beta}^\beta} / R_{\Gamma_{N_\beta}^\beta}^3 + \left[\frac{1 - 2\nu^{\Omega_{N_\beta}^\beta}}{E^{\Omega_{N_\beta}^\beta} \left(R_{\Gamma_{N_\beta-1}^\beta}^3 - R_{\Gamma_{N_\beta}^\beta}^3 \right)} \right. \right. \\ & \times \left(R_{\Gamma_{N_\beta-1}^\beta}^3 \sigma^{\Gamma_{N_\beta-1}^\beta} - R_{\Gamma_{N_\beta}^\beta}^3 \sigma^{\Gamma_{N_\beta}^\beta} \right) + \frac{(1 + \nu^{\Omega_{N_\beta}^\beta}) R_{\Gamma_{N_\beta-1}^\beta}^3}{2E^{\Omega_{N_\beta}^\beta} \left(R_{\Gamma_{N_\beta-1}^\beta}^3 - R_{\Gamma_{N_\beta}^\beta}^3 \right)} \\ & \left. \left. \times \left(\sigma^{\Gamma_{N_\beta-1}^\beta} - \sigma^{\Gamma_{N_\beta}^\beta} \right) \right] \right\} + \frac{(1 + \nu^m) \sigma^{\Gamma_{N_\beta}^\beta}}{3(1 - \nu^m)}, \quad \beta = 1, 2, \dots, P \end{aligned} \tag{19}$$

Equations (14), (15), and (19) contain $2 \sum_{\beta=1}^P N_\beta + 3$ unknown quantities, i.e. $\bar{\sigma}^m$, $\bar{\sigma}$, $\bar{\varepsilon}$, $\Delta_n^{\Gamma_\gamma^\beta}$, and $\sigma^{\Gamma_\gamma^\beta}$ ($\beta = 1, 2, \dots, P$; $\gamma = 1, 2, \dots, N_\beta$); however, there are only $P + 2$ equations. To determine the constitutive relation between the macroscopic stress and the macroscopic strain, it is necessary to consider the cohesive constitutive relation for $\sigma^{\Gamma_\gamma^\beta}$ in terms of $\Delta_n^{\Gamma_\gamma^\beta}$, i.e. equations (11) or (12), which provide another $\sum_{\beta=1}^P N_\beta$ equations. In addition, the relations for radial separations at the debonding interfaces, equations (16) and (17), provide $\sum_{\beta=1}^P N_\beta - P$ equations. Thus, equations (11), (14), (15), (16), (17), and (19) provide a system of algebraic equations which can be solved in terms of separation at only one of the debonding interfaces of multi-phase particles. Using this system of nonlinear algebraic equations, we determine the macroscopic behavior of composite materials accounting for nonlinear interface debonding within multi-phase particles. For illustration of the abovementioned solution procedure, we rewrite the system of equations for the example of a composite material containing two-phase particles with the same size and material properties (i.e. $\beta = 1$, and $\gamma = 1, 2$). Thus, for this composite material, equations (11), (14), (15), (16), (17), and (18), respectively, are rewritten as

$$\begin{aligned} \sigma^{\Gamma_\gamma^1} = & \frac{\phi_n}{\delta_n} \left(\frac{\alpha}{m} \right)^m \left(1 - \frac{\Delta_n^{\Gamma_\gamma^1}}{\delta_n} \right)^{\alpha-1} \left(\frac{m}{\alpha} - \frac{\Delta_n^{\Gamma_\gamma^1}}{\delta_n} \right)^{m-1} \\ & \times (m + \alpha) \frac{\Delta_n^{\Gamma_\gamma^1}}{\delta_n}, \quad \gamma = 1 \text{ and } 2, \\ \Delta_n^{\Gamma_1^1} = & \frac{1 - 2\nu^{\Omega_2^1}}{E^{\Omega_2^1} \left(R_{\Gamma_1^1}^3 - R_{\Gamma_2^1}^3 \right)} \left(R_{\Gamma_1^1}^3 \sigma^{\Gamma_1^1} - R_{\Gamma_2^1}^3 \sigma^{\Gamma_2^1} \right) R_{\Gamma_1^1}^\beta \\ & + \frac{1 + \nu^{\Omega_2^1}}{2E^{\Omega_2^1} \left(R_{\Gamma_1^1}^3 - R_{\Gamma_2^1}^3 \right)} \left(\sigma^{\Gamma_1^1} - \sigma^{\Gamma_2^1} \right) R_{\Gamma_2^1}^3 R_{\Gamma_1^1}^\beta \\ & - \frac{1 - 2\nu^{\Omega_1^1}}{E^{\Omega_1^1}} \sigma^{\Gamma_1^1} R_{\Gamma_1^1}^\beta, \end{aligned}$$

$$\begin{aligned} \bar{\sigma}^m &= \frac{2E^m}{3(1-\nu^m)} \left\{ \Delta_n^{\Gamma_2} / R_{\Gamma_2}^3 + \left[\frac{1-2\nu^{\Omega_2}}{E^{\Omega_2} (R_{\Gamma_1}^3 - R_{\Gamma_2}^3)} \right. \right. \\ &\quad \times \left. \left. \left(R_{\Gamma_1}^3 \sigma^{\Gamma_1} - R_{\Gamma_2}^3 \sigma^{\Gamma_2} \right) + \frac{(1+\nu^{\Omega_2}) R_{\Gamma_1}^3}{2E^{\Omega_2} (R_{\Gamma_1}^3 - R_{\Gamma_2}^3)} (\sigma^{\Gamma_1} - \sigma^{\Gamma_2}) \right] \right\} \\ &\quad + \frac{(1+\nu^m) \sigma^{\Gamma_2}}{3(1-\nu^m)}, \\ \bar{\sigma} &= (1-f) \bar{\sigma}^m + f^{\Omega_1} \sigma^{\Gamma_1} \\ &\quad + \sum_{\alpha=2}^{N_1} f^{\Omega_\alpha} (\sigma^{\Gamma_1} R_{\Gamma_1}^3 - \sigma^{\Gamma_\alpha} R_{\Gamma_\alpha}^3) / (R_{\Gamma_1}^3 - R_{\Gamma_\alpha}^3), \\ \bar{\varepsilon} &= \frac{1-2\nu^m}{E^m} \bar{\sigma} + f^{\Omega_1} \left(\frac{1-2\nu^{\Omega_1}}{E^{\Omega_1}} - \frac{1-2\nu^m}{E^m} \right) \sigma^{\Gamma_1} \\ &\quad + f^{\Omega_2} \left(\frac{1-2\nu^{\Omega_2}}{E^{\Omega_2}} - \frac{1-2\nu^m}{E^m} \right) \\ &\quad \times \left(\sigma^{\Gamma_1} R_{\Gamma_1}^3 - \sigma^{\Gamma_2} R_{\Gamma_2}^3 \right) / (R_{\Gamma_1}^3 - R_{\Gamma_2}^3) + f^{\Omega_2} \frac{\Delta_n^{\Gamma_2}}{R_{\Gamma_2}^3} \end{aligned} \tag{20}$$

Solving this system of algebraic equations, in terms of $\Delta_n^{\Gamma_2}$, we determine the macroscopic stress–strain relation of the corresponding composite material with concurrent debonding at both interfaces.

Illustrative examples and discussion

The microstructural debonding process and macroscopic constitutive behavior of composite materials is investigated through a paired theoretical and computational study. The computational study is conducted on a single coated particle, embedded in a matrix, as illustrated in Figure 4(a). In this model, linear eight-node brick (B8) elements are used to discretize the domain. Mesh refinement studies on the model indicate that meshes with approximately 150,000 bulk elements

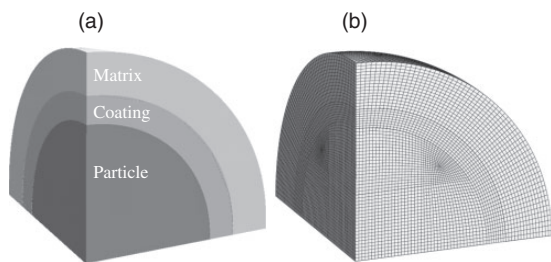


Figure 4. (a) Geometry of the reduced volume element with particle, coating and matrix and (b) finite element mesh of the computational model.

produce accurate results and is the level of refinement used throughout this study, as illustrated in Figure 4(b). At both the particle-coating and coating-matrix interfaces, 3230 cohesive elements are used to capture the debonding phenomena. The insertion of cohesive elements was automated through a MATLAB script which duplicates nodes at the boundary of the particle, and/or interphase, and adjusts the connectivity of the adjacent bulk elements to accommodate the newly inserted cohesive elements. The cohesive elements are implemented as user-defined elements in the commercial software ABAQUS.^{34,35,38} Displacement boundary conditions are applied to the exterior surface of the RVE.

In order to illustrate the diverse applications of the theory, and corresponding model, we now apply it to several complex problems. First, we verify the finite element model by comparing it with a full RVE with multiple particle inclusions. Then, we investigate the effect of many microstructural parameters; including particle size, particle volume fraction, coating thickness, material properties, and cohesive properties. In the following examples, unless stated otherwise, the bulk Poisson’s ratio has been fixed at 0.25, and the cohesive parameters have been fixed at a cohesive fracture energy (ϕ_n) of 1.0 N/m, a cohesive strength (σ) of 15 MPa, a softening shape parameter (α) of 3, and an initial slope indicator (λ_n) of 0.005.

Comparison between the single particle model and a full RVE

In order to verify the use of the finite element model used in this investigation, we compare the response of a single coated particle to that of a full RVE. The RVE is periodic and contains 30 randomly placed particles with a radius of 1 mm. The size of the RVE is such that the particles have a volume fraction of 10%, and an interphase thickness of 0.2 mm, as illustrated in Figure 5. The geometry is meshed with approximately 330,000 linear tetrahedral elements and periodic boundary conditions are applied.^{39,40} The matrix has an elastic modulus of 80 MPa, and the particles have an elastic modulus of 400 MPa. Cohesive elements are inserted between every particle and its corresponding coating and have a cohesive fracture energy of 1.0 N/m, a cohesive strength of 10 MPa, a softening shape parameter of 3, and an initial slope indicator of 0.005. The macroscopic stress–strain behavior of the two different models is compared in Figure 6. As expected, the behavior of the single particle model and the full RVE model is the same under hydrostatic tension. This study is useful to verify the effectiveness of the single particle model and leads to increased confidence in using the simpler model. The single particle model

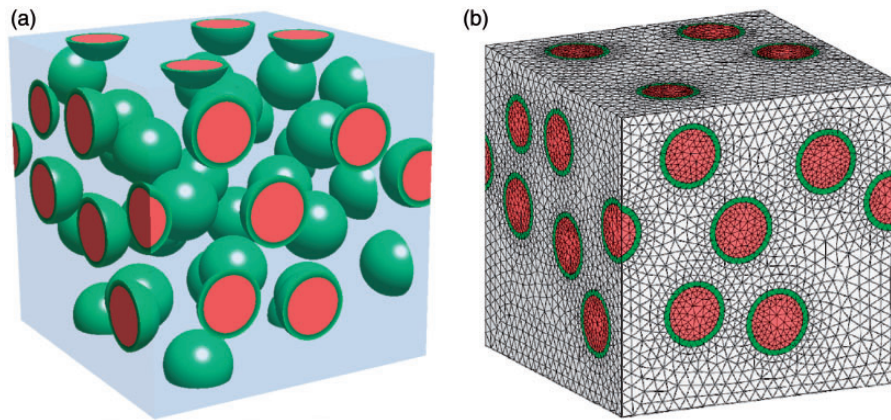


Figure 5. Representative volume element used for verifying the single particle model. (a) Geometry and (b) mesh.

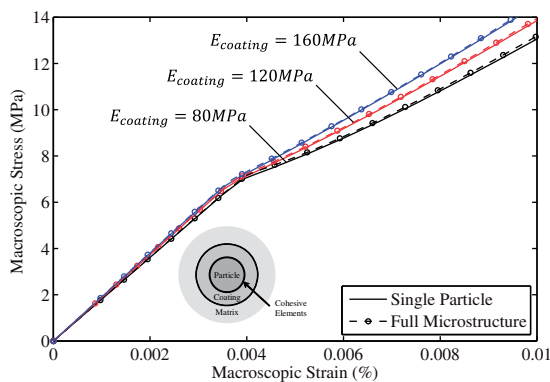


Figure 6. Comparison between the single particle model and the full RVE model. The following properties are considered:

$E_{matrix} = 80 \text{ MPa}$, $E_{particles} = 400 \text{ MPa}$, $f_{particle} = 0.1$,
 $t_{coating} = 0.2 \text{ mm}$, $\sigma_{cohesive} = 10 \text{ MPa}$, $\phi_{cohesive} = 1.0 \text{ N/m}$.

has distinct advantages in this case, as it allows us to model higher volume fractions of the particle ensemble, as the volume fraction of the RVE is limited by the requirement of having a well-formed mesh between particles, and becomes cumbersome once the total volume fraction of the particle ensemble (particles and coatings) exceeds approximately 30%. This limitation is not present in the single particle model. Additionally, the single particle model allows for a direct visualization of the local debonding process, providing a greater understanding of the physical behavior at the microscale. Furthermore, the single particle model allows for a greater resolution (finer mesh) to capture the debonding process at the interface. This becomes significant when the fracture properties are chosen such that they cause the fracture region to reduce in size. When the fracture region is small, the size of the mesh in the RVE grows significantly, and from a computational viewpoint, becomes prohibitive.

Composites with single separation within the inhomogeneity system

We first consider scenarios in which the composite is only permitted to debond at either the particle-coating interface or the coating-matrix interface. The effects due to the location of separation, the geometry of the microstructure, the bulk material properties, and the cohesive properties are investigated.

Rigid particles with homogeneous coating: Separation along the coating-matrix interface. The location of separation greatly influences the overall response of the composite. The first case considers a single location of separation, occurring at the coating-matrix interface. The particle sizes are $R = 0.2 \text{ mm}$ and $R = 1.0 \text{ mm}$, with a fixed particle volume fraction of $f_{particle} = 0.3$. The coating thickness is varied, such that the volume fraction of the coating, $f_{coating}$, equals 0.01, 0.1, 0.2, or 0.4. The matrix has an elastic modulus of 100 MPa, the coating an elastic modulus of 400 MPa, and the particle an elastic modulus of 100 GPa. For the given microstructure, the elastic range and elastic limit is equal for each particle size, with an increasing elastic limit as the thickness of the coating increases, as illustrated in Figure 7. The elastic limit is reached, and separation initiates, once the local stress at the coating-matrix interface reaches the cohesive strength. For the case of coarse particles ($R = 1 \text{ mm}$), the material demonstrates softening behavior past the elastic limit, then gradually transitions to hardening behavior. The magnitude of the softening increases as the thickness of the coating increases, as illustrated in Figure 7(a). For the case of fine particles ($R = 0.2 \text{ mm}$), the material demonstrates hardening behavior past the elastic limit for coatings below $f_{coating} = 0.4$. For the case of $f_{coating} = 0.4$, the material displays softening behavior past the elastic limit, as illustrated in Figure 7(b). The stiffness of the

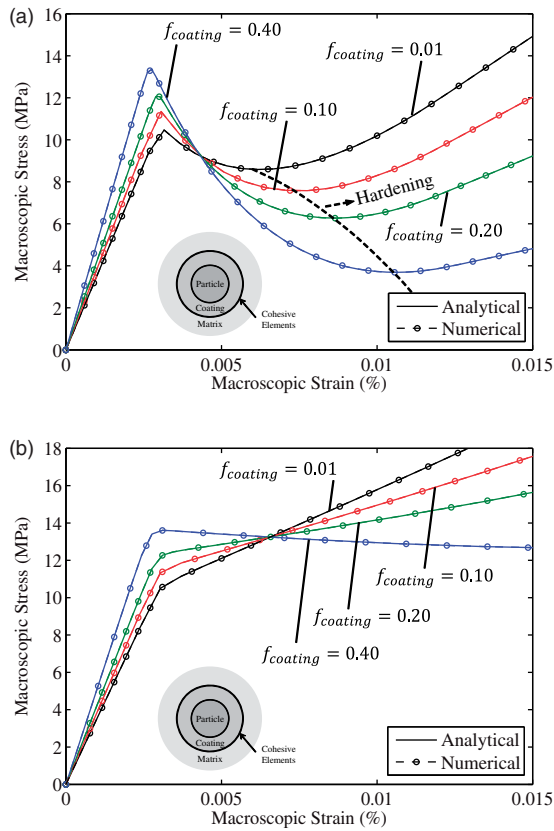


Figure 7. Effect of microstructure on the constitutive response of the composite considering separation along the coating-matrix interface ($E_{particle} = 100$ GPa and $f_{particle} = 0.3$). Particle radius (a) $R = 1$ mm and (b) $R = 0.2$ mm.

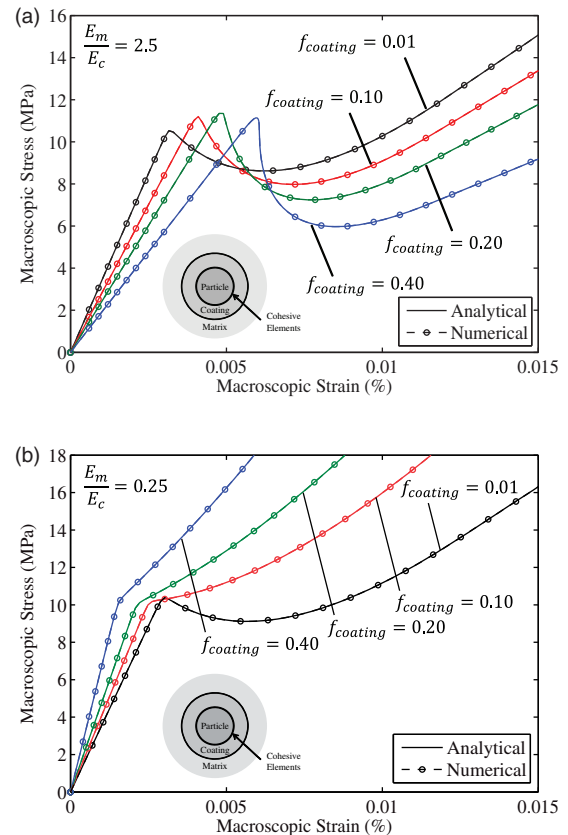


Figure 8. Effect of coating thickness on the constitutive response of the composite considering separation along the particle-coating interface ($R = 1$ mm, $E_{particle} = 100$ GPa and $f_{particle} = 0.3$). Coating modulus of (a) 40 MPa and (b) 400 MPa.

material past the elastic limit increases as the volume fraction of the coating decreases.

Rigid particles with homogeneous coating: Separation along the particle-coating interface. When the location of separation is repositioned to the particle-coating interface, the macroscopic behavior of the material is altered. For this study, the size of the particles is kept constant at $R = 1$ mm, with a fixed volume fraction of $f_{particle} = 0.3$. The elastic modulus of the particle is 100 GPa, and the elastic modulus of the matrix is 100 MPa. The volume fraction and elastic modulus of the coating is varied. When the coating is softer than the surrounding matrix (40 MPa), the elastic stiffness of the material decreases as the volume fraction of the coating increases, as illustrated in Figure 8(a). In all cases, the softer coating leads to softening behavior past the elastic limit. When the coating is stiffer than the matrix (400 MPa), the elastic stiffness of the material increases as the volume fraction of the coating increases; however, the macroscopic stress at the elastic limit is only slightly altered, as

illustrated in Figure 8(b). For a very small coating thickness ($f_{coating} = 0.01$), the material displays softening behavior past the elastic limit; however, as the thickness of the coating increases, the material displays hardening behavior past the elastic limit.

Particles containing centric voids: Separation along the particle-matrix interface. The composition of the particle is important to the overall constitutive response of the composite. This investigation looks at the case when a void is present at the center of the particle. Particles with centric voids are commonly used in the manufacturing of syntactic foams, light weight composites, and self-healing materials.^{41–44} They are particularly suitable when weight considerations are important, such as in the case of the core material in marine and aerospace structures.⁴¹ For this study, we consider two different particle sizes of $R = 0.5$ mm and $R = 1.0$ mm. The elastic modulus for the particle is set at 400 MPa, while that for the matrix is set at 100 MPa. The volume fraction of the void is taken as

a fraction of the volume of the inhomogeneity (particle+void) and is varied from $f_{void} = 0.05$ to $f_{void} = 0.5$. When the volume fraction of the inhomogeneity is $f_i = 0.3$, the response of the material varies as both the size of the particles and the volume fraction of the voids increases, as illustrated in Figure 9(a). When the volume fraction of the voids increases, the elastic stiffness of the material decreases and the elastic limit increases. With coarse particles ($R=1\text{ mm}$), the material displays softening behavior past the elastic limit; whereas, hardening behavior is observed for the case of fine particles ($R=0.5\text{ mm}$). For the case of coarse particles with large voids, snap-back behavior is observed in the post-peak response of the numerical result, indicating an unstable debonding process. When the volume fraction of the inhomogeneity is increased to $f_i = 0.6$, the elastic range of the material decreases and softening behavior is displayed past the elastic limit, as illustrated in Figure 9(b). At large macroscopic strains, complete separation occurs and the load is carried entirely by the matrix shell.

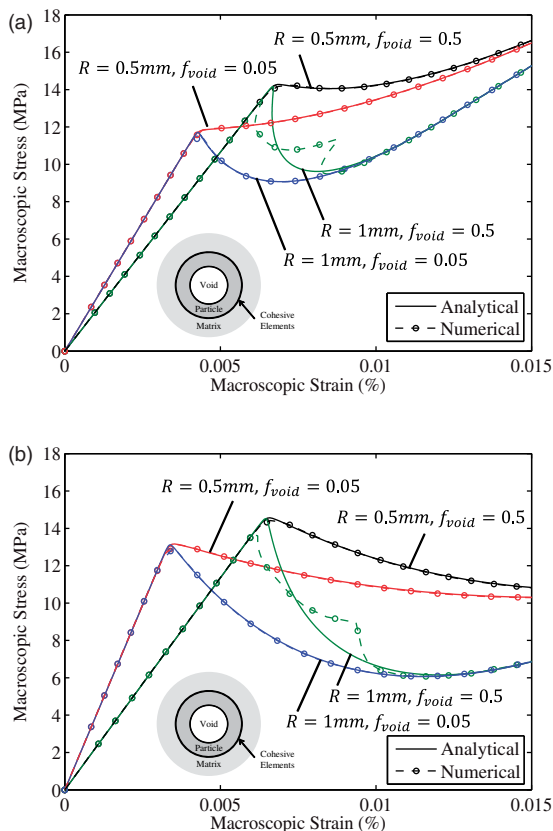


Figure 9. Effect of a void at the center of the particle when the volume fraction of the inhomogeneity (i.e. particle + void) is (a) $f_i = 0.3$ and (b) $f_i = 0.6$. $E_{particle} = 400\text{ MPa}$ and $E_{matrix} = 100\text{ MPa}$.

Particles with functionally graded coating: Separation along the particle-coating interface. The distribution of material in the coating effects the localization of stress at the particle-coating interface. In this study, we investigate the case of heterogeneous coatings with graded elastic modulus in the radial direction. The modulus is linearly varied from that of the particle (400 MPa) to that of the matrix (80 MPa). The particle size is fixed at $R = 1\text{ mm}$, and the effect due to the volume fraction of particle and thickness of coating is investigated. For the case of a thin coating (0.02 mm), as the volume fraction of the particle increases, the elastic stiffness and elastic limit of the material increases, as illustrated in Figure 10(a). In all cases, softening behavior is observed past the elastic limit. As the particle size decreases, complete debonding occurs earlier, and for a volume fraction of 0.1, snap-back behavior is observed in the post-peak response. For thicker coatings (0.2 mm), the influence of the graded coating is increased. Similar to the case with thin coatings, as the volume fraction of the particle increases, the elastic stiffness and elastic limit of the material increases, as illustrated in Figure 10(b).

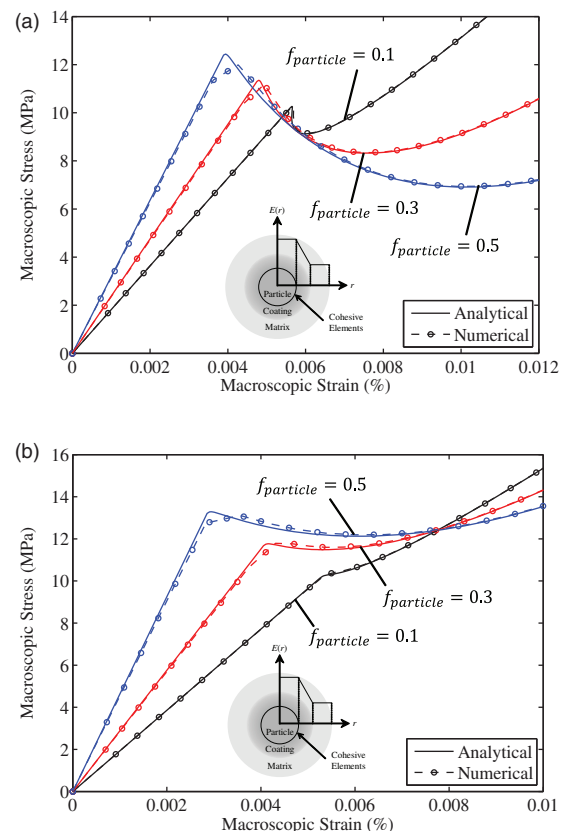


Figure 10. Effect of a functionally graded coating when the coating has a thickness of (a) 0.02 mm and (b) 0.2 mm . $E_{particle} = 400\text{ MPa}$ and $E_{matrix} = 80\text{ MPa}$.

The material generally displays softening behavior past the elastic limit, but transitions to hardening behavior after a small increase in macroscopic strain.

Composites with double concurrent separation within the inhomogeneity system

We now consider scenarios in which concurrent separation is permitted at both the particle-coating interface, and the coating-matrix interface. The effects of the geometry of the microstructure, the material properties, and the cohesive properties are investigated.

Effect of microstructure. Microstructure plays a significant role in the response of the composite. Both the effect of particle size and the effect of coating thickness are investigated. First, the effect of particle size is considered. The particle sizes are chosen as $R = 0.5$ mm, 1 mm, and 1.5 mm, with a fixed particle volume fraction of $f_{particle} = 0.3$, and a fixed coating volume fraction of $f_{coating} = 0.3$. The matrix has an elastic modulus of 100 MPa, the coatings an elastic modulus of 200 MPa, and the particles an elastic modulus of 100 GPa. For this investigation, the cohesive strength is 10 MPa. The initial elastic behavior of the composite is independent of the particle size, as illustrated in Figure 11(a). However, there are two distinct kinks in the stress-strain response of the material. Separation initiates at the particle-coating interface, at a macroscopic stress of approximately 6.8 MPa. Beyond this point, the stiffness of the material decreases with increasing particle size. The second distinct kink in the stress-strain response represents the initiation of separation at the coating-matrix interface. After the coating-matrix interface separates, the material hardens for fine particles ($R = 0.5$ mm), whereas the material softens for coarse particles ($R > 0.5$ mm).

In addition, for a coarse particle ($R = 1$ mm), the effect of coating thickness is investigated. For a particle volume fraction of $f_{particle} = 0.3$, the coating volume fraction is varied ($f_{coating} = 0.15, 0.3, 0.45$). As the volume fraction of the stiff coating increases, the elastic stiffness of the material increases; however, the macroscopic stress at the elastic limit remains the same, as illustrated in Figure 11(b). Separation initiates at the particle-coating interface, followed by that at the coating-matrix interface. For all cases considered, the material displays softening behavior after both interfaces have separated.

Effect of cohesive energies at debonding interfaces. The debonding behavior at each interface depends on the fracture energy of the cohesive model; the larger the fracture energy, the more energy is required to cause debonding. First, the case of a rigid particle

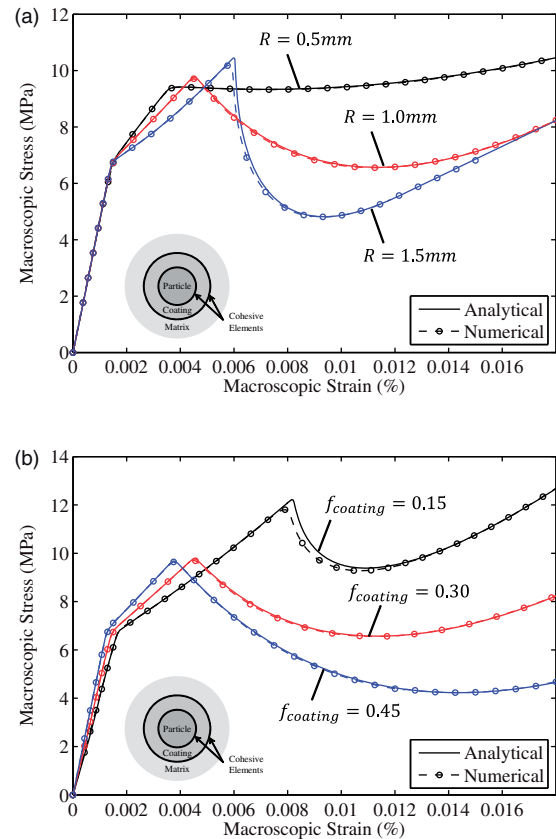


Figure 11. Effect of (a) particle radius and (b) coating thickness. The following properties are considered: $E_{matrix} = 100$ MPa, $E_{coating} = 200$ MPa, $E_{particle} = 100$ GPa, $f_{particle} = 0.3$, $f_{coating} = 0.3$ and $\sigma_{cohesive} = 10$ MPa.

with a stiff coating is considered. The particle size is $R = 1$ mm, with a particle volume fraction of $f_{particle} = 0.3$, and a 0.3 mm thick coating. The matrix has an elastic modulus of 100 MPa, the coating an elastic modulus of 200 MPa, and the particle an elastic modulus of 100 GPa. The cohesive strength is 10 MPa and the fracture energy is varied. The particle-coating interface separates first, at a macroscopic stress of approximately 6.8 MPa, as illustrated in Figure 12(a). As the fracture energy at this interface increases, the stiffness of the subsequent material increases. The coating-matrix interface separates second, and the material displays softening behavior past the elastic limit. The rate at which the material displays softening behavior increases with decreasing fracture energy at the coating-matrix interface.

In addition, we consider the case of particles which are softer than both the coating and the matrix. The geometry of the microstructure remains the same, but now the elastic modulus of the matrix is 150 MPa, the elastic modulus of the coating is 110 MPa, and the elastic modulus of the particle is 80 MPa. Although cohesive elements are inserted at both interfaces, the

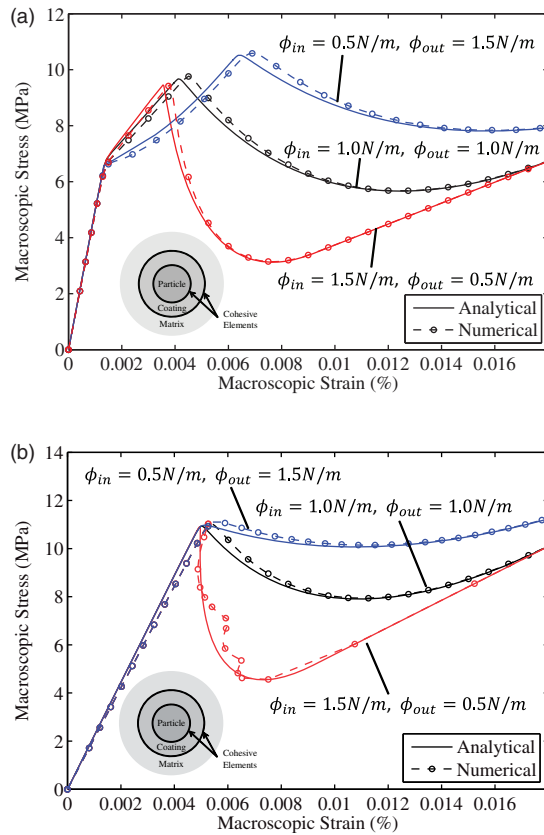


Figure 12. Effect of cohesive fracture energy for (a) rigid particles and (b) softer particles. The properties for each case are: (a) $E_{matrix} = 100$ MPa, $E_{coating} = 200$ MPa, $E_{particle} = 100$ GPa, $f_{particle} = 0.3$ and $\sigma_{cohesive} = 10$ MPa; (b) $E_{matrix} = 150$ MPa, $E_{coating} = 110$ MPa, $E_{particle} = 80$ MPa, $f_{particle} = 0.3$, and $\sigma_{cohesive} = 10$ MPa.

material only separates at the coating-matrix interface, as illustrated by the presence of a single kink in the stress-strain response in Figure 12(b). The fracture energy does not alter the elastic behavior of the material. Beyond the elastic limit, the material displays softening behavior, the rate of which increases with decreasing fracture energy, indicating a more brittle behavior.

Effect of cohesive strengths at debonding interfaces. The effect of the cohesive strength on the behavior of the material is investigated. The particle size is set as $R = 1$ mm, with a volume fraction of $f_{particle} = 0.3$, and a coating thickness of 0.3 mm. The particle, coating, and matrix have an elastic modulus of 100 GPa, 200 MPa, and 100 MPa, respectively. The cohesive strengths for the two interfaces are varied independently. When the strength of the particle-coating interface is set to 15 MPa, the material separates at the coating-matrix interface, and no separation occurs at the particle-coating interface, as demonstrated by the

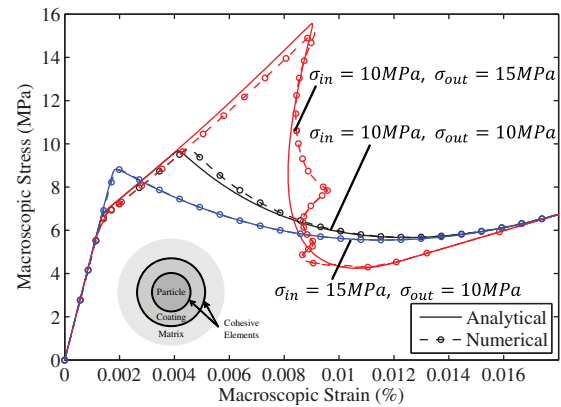


Figure 13. Effect of cohesive strength on the constitutive relationship.

single kink in the response illustrated in Figure 13. However, when the strength of the particle-coating interface is set to 10 MPa, the material separates at the particle-coating interface first then at coating-matrix interface. Beyond the elastic limit, the material displays softening behavior in all cases considered. At large macroscopic strains, complete separation occurs and the load is carried entirely by the matrix shell.

Remarks on results

The results from both the theoretical and computational models agree well with one another. The initial, elastic region is captured exactly in all cases. In general, the elastic limit (the point at which separation initiates) is captured, and the post peak behavior is represented well. When the chosen cohesive parameters lead to very brittle behavior, represented by rapid changes in stress with small increases in strain, the results from the finite element model deviate slightly from those captured theoretically. Through this thorough parametric study, we have illustrated the significant effect that a coating has on the overall macroscopic behavior of composite materials.

Discussion of extensions

While the current formulation focuses on the important case of hydrostatic tension, the numerical model is general and can be extended to any case of loading or underlying material. In this section, we motivate the extension of this work, by numerically considering the case of a composite material with coated particle inclusions loaded in uniaxial tension. Under uniaxial tension, the debonding behavior of the matrix from the particle is nonuniform, going through gradual stages of partial debonding, as observed experimentally and illustrated in Figure 14.

The problem of uniaxial tension of linear elastic materials, accounting for debonding, has been investigated by numerous researchers. Needleman⁴⁶ developed a cohesive model and applied it to the problem of inclusion debonding of a particle reinforced composite. He was able to capture the partial debonding and stress redistribution behavior around the particle. Levy⁴⁷ investigated nonlinear interfacial debonding of a fiber reinforced composite material using a single composite cylinder. Tan et al.²⁶ extended the Mori–Tanaka method to the case of uniaxial tension, accounting for interface debonding using a linear softening cohesive relation. None of the above investigations considered the influence of a coating (or interphase) between the particle and the matrix; however, Shodja and Sarvestani,⁴⁸ Shodja and Roumi,⁷ and Hatami-Marbini and Shodja⁴⁹ have demonstrated

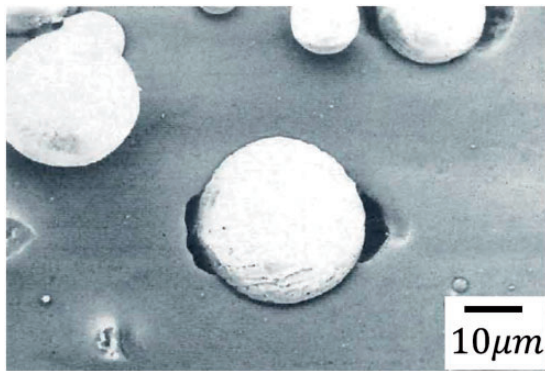


Figure 14. Experimental observation of interface debonding in a metal matrix composite undergoing uniaxial tension, Kanetake et al.⁴⁵

that there are significantly different elastic fields around such inclusions, affecting the behavior of debonding.

Uniaxial tension with separation along the particle-coating interface

The first scenario we consider investigates progressive debonding at the particle-coating interface. The geometry and mesh of the model is illustrated in Figure 15. The particle has a volume fraction of 20%, with a diameter of 1 mm, and the coating is 0.1 mm thick. The matrix has an elastic modulus of 80 MPa, and the particle has an elastic modulus of 400 MPa. Cohesive elements are inserted between the particle and the matrix and have a cohesive fracture energy of 1.0 N/m, a cohesive strength of 15 MPa, a softening shape parameter of 3, and an initial slope indicator of 0.005. The finite element mesh contains approximately 100,000 linear tetrahedral elements to model the bulk material and 3765 cohesive elements to capture the debonding behavior. Rollers are placed on the faces corresponding to the planes of symmetry, and the lateral extension is displacement controlled, as illustrated in Figure 15.

The results of the analysis are illustrated in Figure 16. When the coating is introduced, the elastic stiffness and elastic limit increase slightly. However, the most significant influence of the coating is in the post-peak behavior of the composite. Without the coating, the composite displays a small region of softening prior to an extended region of hardening. The cases which include a coating display hardening behavior past the elastic limit. In comparison to the hydrostatic loading cases considered throughout the rest of the paper, the global strain at the elastic limit is two to three times greater than that

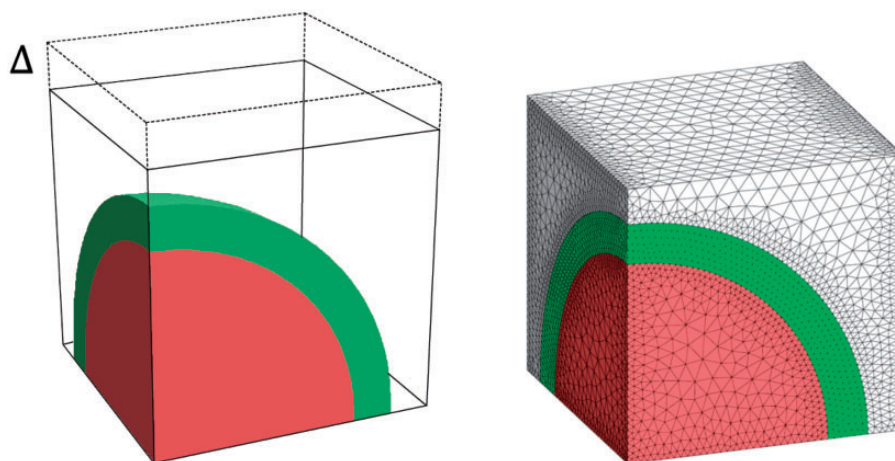


Figure 15. Single particle model used for uniaxial tension simulations. (a) Geometry illustrating the displacement controlled lateral displacement and (b) mesh.

seen in comparable hydrostatic loading cases. As well, the transition between the elastic range and the debonded range is more gradual in the case of uniaxial tension, because the debonding occurs gradually, initiating at the pole of the particle and propagating down to the equator, as illustrated in Figure 17.

Uniaxial tension with separation at both the particle-coating and coating-matrix interfaces

For additional motivation, we consider a scenario in which concurrent separation is permitted at both the particle-coating interface and coating-matrix interface. The same bulk mesh is selected for this study, with an additional 5812 cohesive elements inserted between the coating and the matrix. All the cohesive elements have a cohesive fracture energy of 1.0 N/m, a softening shape parameter of 3, and an initial slope indicator of

0.005. The cohesive strength is 8 MPa and 12 MPa at the particle-coating and coating-matrix interfaces, respectively.

The results of the analysis are illustrated in Figure 18. The “no coating” case corresponds to a coating layer with the properties of the matrix. As with the single separation case, when the coating is introduced, the elastic stiffness and elastic limit increase slightly. There are two distinct kinks in the stress–strain response of the material. Separation initiates at the particle-coating interface, at a macroscopic stress of approximately 10 MPa. Beyond this point, the stiffness of the material decreases with decreasing coating modulus. The second distinct kink in the stress–strain response represents the initiation of separation at the coating-matrix interface. After the coating-matrix

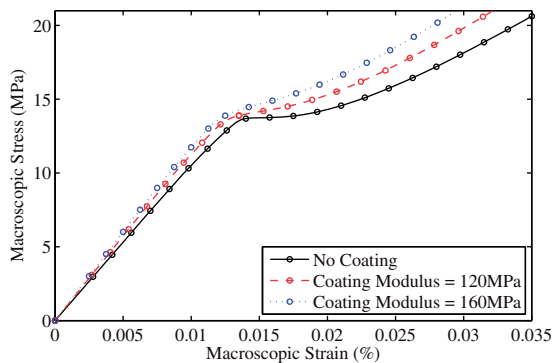


Figure 16. Constitutive response for the coated particle composite loaded in uniaxial tension, demonstrating the influence of the coating when separation is permitted at the particle-coating interface. The following properties are considered: $E_{matrix} = 80$ MPa, $E_{particles} = 400$ MPa, $f_{particle} = 0.2$, $t_{coating} = 0.1$ mm, $\sigma_{cohesive} = 15$ MPa, $\phi_{cohesive} = 1.0$ N/m.

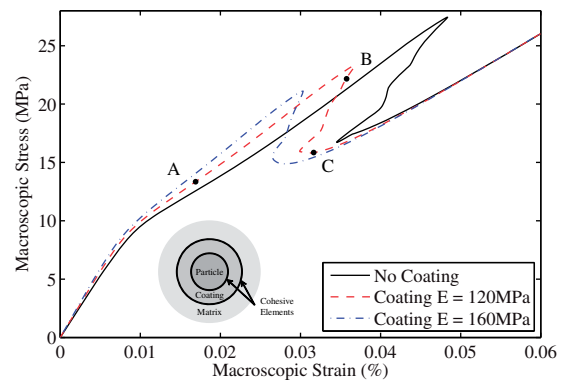


Figure 18. Constitutive response for the coated particle composite loaded in uniaxial tension, demonstrating the influence of the coating when separation is permitted at both the particle-coating and coating-matrix interfaces. The following properties are considered: $E_{matrix} = 80$ MPa, $E_{particles} = 400$ MPa, $f_{particle} = 0.2$, $t_{coating} = 0.1$ mm, $\sigma_{cohesive} = 10$ MPa, $\phi_{cohesive} = 1.0$ N/m. The configurations A, B, and C are illustrated in Figure 19.

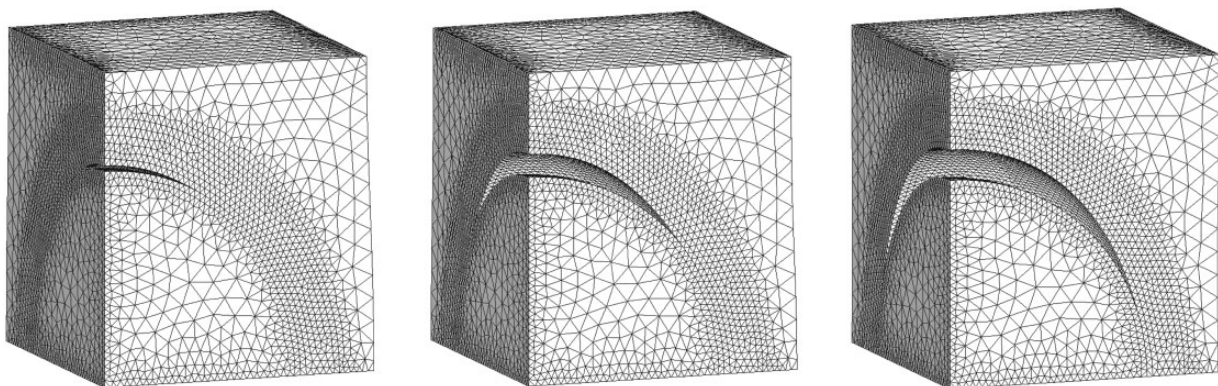


Figure 17. Progression of debonding of a coated particle under uniaxial tension when separation is permitted at the particle-coating interface. Displacements scaled by a factor of 10, for illustrative purposes.

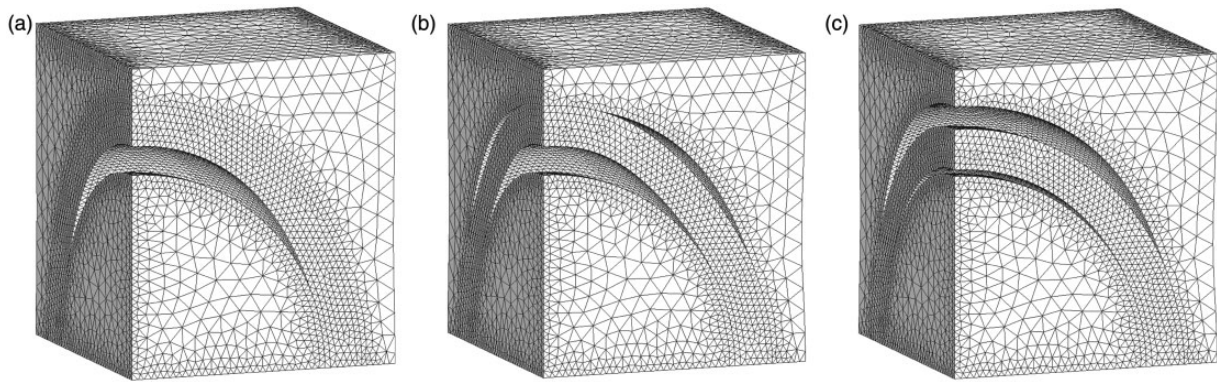


Figure 19. Progression of debonding of a coated particle under uniaxial tension when separation is permitted at both the particle-coating and coating-matrix interfaces. Displacements scaled by a factor of 10, for illustrative purposes. The configurations A, B, and C are illustrated in Figure 18 for the constitutive response.

interface separates, the material displays snap-back behavior in all cases considered. At large macroscopic strains, complete separation occurs, and the load is carried entirely by the matrix shell. The progression of debonding is illustrated in Figure 19.

Conclusion

The macroscopic response of composite materials with multi-coated particles is investigated through a paired theoretical and computational study. We have used the extended Mori–Tanaka model for the theoretical micromechanics investigation, while the computational study uses three-dimensional finite element models with intrinsic cohesive elements. The cohesive elements follow the PPR potential-based cohesive zone model, capturing the nonlinear debonding process at the interface, and are implemented in the commercial finite element software ABAQUS. The change in the macroscopic behavior due to changes in the microstructure is the focus of this investigation. The effects due to variation in volume fraction of particles, in coating thickness, in material properties, in cohesive properties, and in location of separation are investigated. In general, when separation is permitted at a single interface (either the particle-coating or coating-matrix interface), the behavior captured numerically agrees well with that captured theoretically (Figures 7 to 10). Depending on the material properties, when multiple interfaces are permitted to separate, the particle-coating interface tends to separate first, followed by the coating-matrix interface, resulting in two distinct kinks in the stress-strain response (Figures 11 to 13). When the macroscopic stress-strain response displays softening or hardening behavior, the debonding process is stable, whereas when the response displays snap-back behavior, the debonding process demonstrates instabilities. Overall, the results from the computational study

correlate very well with those from the theoretical study and provide insight to the debonding process of composite materials with multi-coated particles. The natural extension of this work is to consider additional loading cases and constitutive relations. The extension of the numerical model to uniaxial tension illustrates progressive debonding behavior regardless of the location of separation.

Author contribution

Roohollah Hashemi and Daniel W Spring contributed equally to this work.

Funding

We acknowledge support from the National Science Foundation, under grants #1031218, #1321661, and #1437535. Daniel W Spring gratefully appreciates the support of the Natural Sciences and Engineering Research Council of Canada. We also acknowledge support from the Donald and Elizabeth Willett endowment at the University of Illinois at Urbana-Champaign (UIUC). The opinions expressed are solely those of the authors and do not necessarily reflect the views of the sponsors or sponsoring agencies.

Conflict of interest

None declared.

Acknowledgements

We thank Professor Marco Alfano (University of Calabria) for helpful discussion regarding the content of this manuscript.

References

1. Qu M, Deng F, Kalkhoran SM, et al. Nanoscale visualization and multiscale mechanical implications of bound rubber interphases in rubber-carbon black nanocomposites. *Soft Matter* 2011; 7: 1066–1077.

2. Nemat-Nasser S and Hori M. *Micromechanics: overall properties of heterogeneous materials, second edition*. The Netherlands: Elsevier, 1993.
3. Hori M and Nemat-Nasser S. Double-inclusion model and overall moduli of multi-phase composites. *J Eng Mater Tech* 1994; 116: 305–309.
4. Dunn ML and Ledbetter H. Elastic moduli of composites reinforced by multiphase particles. *J Appl Mech* 1995; 62: 1023–1028.
5. Kalamkarov AL and Kolpakov AG. *Analysis, design and optimization of composite structures*, 2nd ed. Chichester, England: John Wiley & Sons Ltd, 1997.
6. EI Mouden M, Cherkaoui M, Molinari A, et al. The overall elastic response of materials containing coated inclusions in a periodic array. *Int J Eng Sci* 1998; 36: 813–829.
7. Shodja HM and Roumi F. Overall behavior of composites with periodic multi-inhomogeneities. *Mech Mater* 2005; 37: 343–353.
8. Hashemi R, Weng GJ, Kargarnovin MH, et al. Piezoelectric composites with periodic multi-coated inhomogeneities. *Int J Solids Struct* 2010; 47: 2893–2904.
9. Bertoldi K and Lopez-Pamies O. Some remarks on the effect of interphases on the mechanical response and stability of fiber-reinforced composites. *J Appl Mech* 2012; 79: 031023.
10. Han F, Azdoud Y and Lubineau G. Computational modeling of elastic properties of carbon nanotube/polymer composites with interphase regions. Part I: micro-structural characterization and geometric modeling. *Comput Mater Sci* 2014; 81: 641–651.
11. Han F, Azdoud Y and Lubineau G. Computational modeling of elastic properties of carbon nanotube/polymer composites with interphase regions. Part II: mechanical modeling. *Comput Mater Sci* 2014; 81: 652–661.
12. Mura T and Furuhashi R. The elastic inclusion with a sliding interface. *ASME J Appl Mech* 1984; 51: 308–310.
13. Mura T. *Micromechanics of defects in solids*, 2nd, revised ed. The Netherlands: Kluwer Academic Publishers, 1991.
14. Tan H, Huang Y, Liu C, et al. The Mori–Tanaka method for composite materials with nonlinear interface debonding. *Int J Plast* 2005; 21: 1890–1918.
15. Crouch SL and Mogilevskaia SG. Loosening of elastic inclusions. *Int J Solids Struct* 2006; 43: 1638–1668.
16. Duan HL, Yi X, Huang ZP, et al. A unified scheme for prediction of effective moduli of multiphase composites with interface effects. Part I: theoretical framework. *Mech Mater* 2007; 39: 81–93.
17. Brassart L, Inglis HM, Delannay L, et al. An extended Mori–Tanaka homogenization scheme for finite strain modeling of debonding in particle-reinforced elastomers. *Comput Mater Sci* 2009; 45: 611–616.
18. Benveniste Y. The effective mechanical behavior of composite materials with imperfect contact between the constituents. *Mech Mater* 1985; 4: 197–208.
19. Achenbach JD and Zhu H. Effect of interfacial zone on mechanical behavior and failure of fiber-reinforced composites. *J Mech Phys Solids* 1989; 37: 381–393.
20. Sangani AS and Mo G. Elastic interactions in particulate composites with perfect as well as imperfect interfaces. *J Mech Phys Solids* 1997; 45: 2001–2031.
21. Nie S and Basaran C. A micromechanical model for effective elastic properties of particulate composites with imperfect interfacial bonds. *Int J Solids Struct* 2005; 42: 4179–4191.
22. Schjudt T and Pyrz R. Overall creep modelling of short fibre reinforced composites with weakened interfaces and complex fibre orientation. *Mech Mater* 2000; 32: 349–359.
23. Lee HK and Pyo SH. Micromechanics-based elastic damage modeling of particulate composites with weakened interfaces. *Int J Solids Struct* 2007; 44: 8390–8406.
24. Xu XP and Needleman A. Void nucleation by inclusion debonding in a crystal matrix. *Modell Simul Mater Sci Eng* 1993; 1: 111–132.
25. Tan H, Huang Y, Liu C, et al. The uniaxial tension of particle-reinforced composite materials with nonlinear interface debonding. *Int J Solids Struct* 2007; 44: 1809–1822.
26. Tan H, Huang Y, Liu C, et al. Constitutive behaviors of composites with interface debonding: the extended Mori–Tanaka method for uniaxial tension. *Int J Fract* 2007; 146: 139–148.
27. Carpinteri A, Paggi M and Zavarise G. Snap-back instability in micro-structured composites and its connection with superplasticity. *Strength Fract Complex* 2005; 3: 61–72.
28. Ngo D, Park K, Paulino GH, et al. On the constitutive relation of materials with microstructure using a potential-based cohesive model for interface interaction. *Eng Fract Mech* 2010; 77: 1153–1174.
29. Othmani Y, Delannay L and Doghri I. Equivalent inclusion solution adapted to particle debonding with a nonlinear cohesive law. *Int J Solids Struct* 2011; 48: 3326–3335.
30. Mori T and Tanaka K. Average stress in matrix and average elastic energy of materials with misfitting inclusions. *Acta Metall* 1973; 21: 571–574.
31. Weng GJ. Some elastic properties of reinforced solids with special reference to isotropic ones containing spherical inclusions. *Int J Eng Sci* 1984; 22: 845–856.
32. Qiu YP and Weng GJ. On the application of Mori–Tanaka’s theory involving transversely isotropic inclusions. *Int J Eng Sci* 1990; 28: 1121–1137.
33. Park K, Paulino GH and Roesler JR. A unified potential-based cohesive model for mixed-mode fracture. *J Mech Phys Solids* 2009; 57: 891–908.
34. Park K and Paulino GH. Computational implementation of the PPR potential-based cohesive model in ABAQUS: educational perspective. *Eng Fract Mech* 2012; 92: 239–262.
35. Spring DW and Paulino GH. A growing library of three-dimensional cohesive elements for use in ABAQUS. *Eng Fract Mech* 2014; 126: 190–216.
36. Timoshenko S and Goodier JN. *Theory of elasticity*, 3rd ed. New York: McGraw-Hill, 1970.

37. Phan-Thien N and Kim S. *Microstructures in elastic media: Principles and computational methods*. New York: Oxford University Press, 1994.
38. ABAQUS Version 6.11 Documentation, 2011. Dassault Systemes Simulia Corp., Providence, RI, USA.
39. Miehe C. Computational micro-to-macro transitions for discretized micro-structures of heterogeneous materials at finite strains based on the minimization of averaged incremental energy. *Comput Methods Appl Mech Eng* 2003; 192: 559–591.
40. Okereke MI and Akpoyomare AI. A virtual framework for prediction of full-field elastic response of uni-directional composites. *Comput Mater Sci* 2013; 70: 82–99.
41. Low LF and Abu Baker A. Advanced hollow epoxy particle-filled composites. *J Compos Mater* 2011; 45: 2287–2299.
42. Liu JA, Yu SR, Huang ZQ, et al. Microstructure and compressive property of in situ Mg₂Si reinforced Mg-microballoon composites. *J Alloys Compd* 2012; 537: 12–18.
43. Porfiri M and Gupta N. Effect of volume fraction and wall thickness on the elastic properties of hollow particle filled composites. *Compos Part B* 2009; 40: 166–173.
44. Liang JZ. Impact fracture toughness of hollow glass bead-filled polypropylene composites. *J Mater Sci* 2007; 42: 841–846.
45. Kanetake N, Nomura M and Choh T. Continuous observation of microstructural degradation during tensile loading of particle reinforced aluminum matrix composites. *Mater Sci Tech* 1995; 11: 1246–1252.
46. Needleman A. A continuum model for void nucleation by inclusion debonding. *J Appl Mech* 1987; 54: 525–531.
47. Levy AJ. The fiber composite with nonlinear interface – Part I: axial tension. *J Appl Mech* 2000; 67: 727–732.
48. Shodja HM and Sarvestani AS. Elastic fields in double inhomogeneity by the equivalent inclusion method. *J Appl Mech* 2001; 68: 3–10.
49. Hatami-Marbini H and Shodja HM. Effects of interface conditions on thermo-mechanical fields of multi-phase nano-fibers/particles. *J Therm Stresses* 2009; 32: 1166–1180.